

This is the accepted manuscript of the following article: Lam, K. C., Huang, B., & Shi, S.-Q. (2017). Room-temperature methane gas sensing properties based on in situ reduced graphene oxide incorporated with tin dioxide. *Journal of Materials Chemistry A*, 5(22), 11131-11142, which has been published in final form at <https://doi.org/10.1039/C7TA01293D>.



Journal of Materials Chemistry A

PAPER

Room temperature methane gas sensor based on in-situ reduced graphene oxide incorporated with tin dioxide

King Cheong Lam,^a Bolong Huang^b and San Qiang Shi^{*a}

Received 00th January 20xx,
Accepted 00th January 20xx

DOI: 10.1039/x0xx00000x

www.rsc.org/

We report on the relationship between the degree of reduction of graphene oxide (GO) and its room-temperature methane gas-sensing response by comparing four in situ reducing agents of GO: D-glucose, sodium borohydride, L-ascorbic acid and hydrazine hydrate. We found that gas sensors based on D-glucose and L-ascorbic acid had a higher gas response than those based on sodium borohydride and hydrazine hydrate because the residues contained oxygen functional groups. The poorly conductive GO was successfully reduced in situ by L-ascorbic acid to achieve high electrical conductivity and high methane gas response. The incorporation of tin dioxide (SnO₂) into the reduced GO (RGO) further increased the gas response by the p-n junction effect. The heterostructure of L-ascorbic acid-reduced RGO-SnO₂ had the highest increase in methane response due to the synergistic effect between dehydroascorbic acid and the SnO₂ surface. This was inferred from density functional theory calculations with self-consistently determined Hubbard U potentials (DFT+U). Compared with the current room-temperature methane sensors and fabrication technologies, the sensor reported here is cheaper to produce and more environmentally friendly while retaining high sensitivity.

1. Introduction

Among metal oxide semiconductor gas sensors, tin dioxide (SnO₂) has been intensively studied for its advantages of high gas sensitivity, stability and fast response.^{1–3} SnO₂ is an n-type semiconductor due to the oxygen vacancy defects on the surface, which serve as active sites for gas sensing to induce a high gas response. The addition of metallic particles such as palladium (Pd) or platinum (Pt) to SnO₂ has been reported to have increased gas sensitivity via chemical and electronic additive effects.^{4–6} However, in general, metal oxide gas sensors have drawbacks, including a high operating temperature and high power consumption. To improve the conductivity of metal oxides, alternative additive materials such as reduced graphene oxide (RGO) have recently been explored for their advantages of high sensitivity, fast response and good conductivity.^{7–11} As a frontier material, graphene is of particular interest in applications such as solar cells and gas sensors due to its superior electrochemical properties. Graphene is a two-dimensional and single-layer sheet of sp² hybridised carbon atoms with zero band gap energy, which possesses superior electrical conductance. It demonstrates ambipolar effects, allowing the type of charge carrier to be tuned by adjusting the gate voltage. Moreover, graphene can be considered an ideal electrode material because of its large surface area, superior electrical conductance and fast electron transfer rate. The

specific surface area of graphene is ~2,600 m²/g, about twice as large than that of carbon nanotubes (CNTs).¹² Moreover, the widely open structure enables it to have a faster response than CNTs. Currently, gas sensors based on graphene-related materials are being intensively studied due to their high sensitivity, selectivity and fast response to a variety of gases.¹³ However, the pristine form of graphene has been reported to have low gas sensitivity due to the lack of energetically favourable sites, such as defects or functional groups, to interact with gases.¹⁴

Graphene oxide (GO), the oxidised form of graphene, contains abundant defect sites as well as oxygen functional groups on the graphitic plane.¹⁵ A gas sensor based on GO has been reported to have a high gas response due to the presence of energetically favourable sites to interact with gases.¹⁶ GO has further advantages over pristine graphene, including the ability to disperse in polar solvents such as water or alcohol due to the formation of hydrogen bonds between the solvent and the oxygen functional groups on GO. However, the defects and functional groups on GO also destroy the continuity of the ballistic transport of charge carriers on the graphitic plane.¹⁷ Hence, GO is poorly conductive, which restrains its electrical applications. The modification of GO is mostly based on chemical reduction to reduced GO (RGO) to improve its conductivity without a significant loss of defect sites.¹⁸ Reduction of GO by different reducing agents has been reported in the development of sensors with various sensitivities towards different gases. For example, hydrazine hydrate is commonly used due to its strong reducing power.^{19,20} However, it is highly toxic, and the focus has now shifted to producing RGO using less toxic and more environmentally friendly reagents such as sodium borohydride, L-ascorbic acid (vitamin C) and D-

^a Department of Mechanical engineering, The Hong Kong Polytechnic University, Hong Kong. E-mail: san.qiang.shi@polyu.edu.hk; Fax: (852) 2364-7183; Tel: (852) 27667821

^b Department of Applied Biology and Chemical Technology, The Hong Kong Polytechnic University, Hong Kong. E-mail: bhuang@polyu.edu.hk; Fax: (852) 2364 9932; Tel: (852) 3400 8679

glucose.^{21–23} The hybridisation of RGO with metal oxides such as SnO₂ has been reported to greatly increase the gas sensitivity at much lower operating temperatures^{24,25} due to the high conductivity of RGO. In addition to inducing good responsiveness, the addition of SnO₂ is far more economical than the use of noble transition metals such as Pd or Pt. Hence, sensors based on heterostructures of RGO and SnO₂ are expected to have stronger and faster gas responses.

Methane gas is the main component of natural gas, biogas and fuel gas. It is non-toxic and odourless but highly flammable in air. The explosion limits of methane have been determined as 4.7–16.3% in air.²⁶ Even small leakages can cause explosions, as occurs in many environmental accidents such as coal mining accidents. Methane is extremely difficult to detect at trace amounts due to the non-polarity and high enthalpy of the C-H bond.²⁷ Hence, the development of a low-temperature methane gas sensor remains an active research goal.

As different reducing agents produce forms of RGO with different gas-sensing properties, a promising approach is to search for an optimal reducing agent combining high electrical conductivity with a high gas response. In this work, GO obtained by the modified Hummers method was reduced by four agents: D-glucose, sodium borohydride, L-ascorbic acid and hydrazine hydrate. SnO₂ was then incorporated into the resulting RGO to further increase their room-temperature gas response and conductivity. The morphology, degree of reduction and crystallinity of the homostructures and heterostructures were characterised by SEM, Raman spectroscopy, FTIR spectroscopy and XRD. The resistance and methane response of the different composites were compared.

2. Experimental

A schematic diagram of the preparation of the heterostructured RGO-SnO₂ composite is shown in Fig. 1. First, GO was prepared using the modified Hummers method.²⁸ The following typical procedure was adopted: 1.0 g of graphite flakes (1,000 mesh) was mixed with 25 ml of concentrated sulphuric acid (96%) with vigorous stirring for 15 min. Then, 1.25 g of sodium nitrate was added to the suspension with vigorous stirring for 1 h. Then, 3.7 g of potassium permanganate was added to the suspension and stirred constantly for 3 h at the elevated temperature of 35°C. During this process effervescence occurred and a dark brown slurry paste was formed. Then, 60 ml of icy water was added gradually to the slurry paste and stirred constantly until no bubbles evolved. The slurry paste turned light brown in colour. Then, the slurry paste was further diluted with 140 ml of icy water and stirred constantly until no bubbles evolved. Finally, 30 ml of hydrogen peroxide (35%) was added to the slurry paste and the colour immediately changed from light brown to bright yellow. The paste was then filtered and washed with a solution of 50 ml of D.I. water and 20 ml of hydrochloric acid (1N) three times. Finally, the filtered light brown cake was dried at 60°C overnight in an oven.

The GO obtained was reduced in situ by D-glucose (G), sodium borohydride (B), L-ascorbic acid (A) and hydrazine hydrate (H) in separate experiments. Typically, 0.15 g of GO was

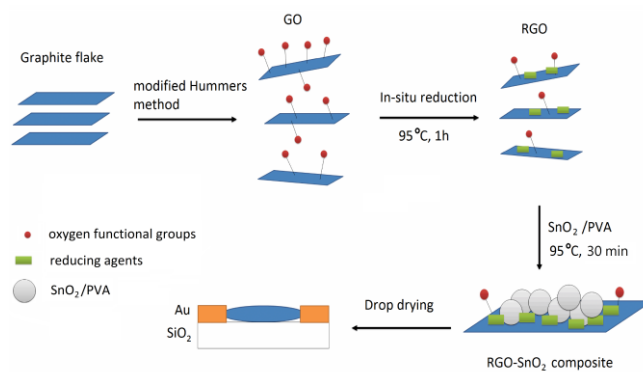


Fig. 1 Schematic diagram for preparation of RGO-SnO₂ composite

dispersed in 15 ml of D.I. water with stirring for 1 h and sonication for 1 h. Then, 0.1 g of D-glucose (for example) was added to the suspension and stirred for 1 h with heating at 95°C. Then, 0.6 g SnO₂ and 0.01 g polyvinyl alcohol (PVA) powders were added to the reduced suspension with vigorous stirring and heating at 95°C for 30 min. A small amount of PVA was added as a binder and homogeniser to disperse the SnO₂ crystallites uniformly in the suspension. The same reduction procedure followed by an incorporation of SnO₂ was followed for the sodium borohydride, L-ascorbic acid and hydrazine hydrate. The RGO reduced by D-glucose, sodium borohydride, L-ascorbic acid and hydrazine hydrate was designated as R(G), R(B), R(A) and R(H), respectively. Gas sensors were fabricated by drop-drying the composite solutions onto a glass substrate with gentle heating at 120°C for 15 min. A pair of gold electrodes with a separation of 5 mm was sputtered onto the surfaces of the samples for sensor tests.

3. Results and discussion

3.1. SEM analysis

Representative SEM images of the homostructures of GO and R(A) and all of the heterostructures are shown in Fig. 2. Fig. 2(a) shows that in the GO, stacked layers of GO platelets of different sizes were aggregated and randomly distributed over each other. Fig. 2 (b) shows that the RGO platelets in R(A) were more aggregated than the GO platelets. This aggregation was due to the recovery of the π - π interaction between the graphitic planes after reduction by removing the electrostatically repelling oxygen functional groups on the GO.¹⁸ Fig. 2(c) shows that dispersed SnO₂ nanocrystallites with sizes of 50–70 nm were uniformly distributed on the R(G) platelets. Fig. 2(d) shows that the composites of R(B) and SnO₂ were firmly aggregated, with a partially transparent film of PVA. Film-like structures could be formed by crosslinking PVA polymers via a solvolysis reaction between the borohydride and hydroxyl group of PVA.^{29,30} However, the film-like structure of PVA was not favourable for gas sensing, as it screened the gas from passing into the sensing elements of the composites. Fig. 2(e) shows that the composites of R(A) and SnO₂ were more aggregated, with larger platelets, due to the greater degree of reduction of R(A). Fig. 2(f) shows that the composites of R(H) and SnO₂ were mostly stacked and aggregated, evidencing that

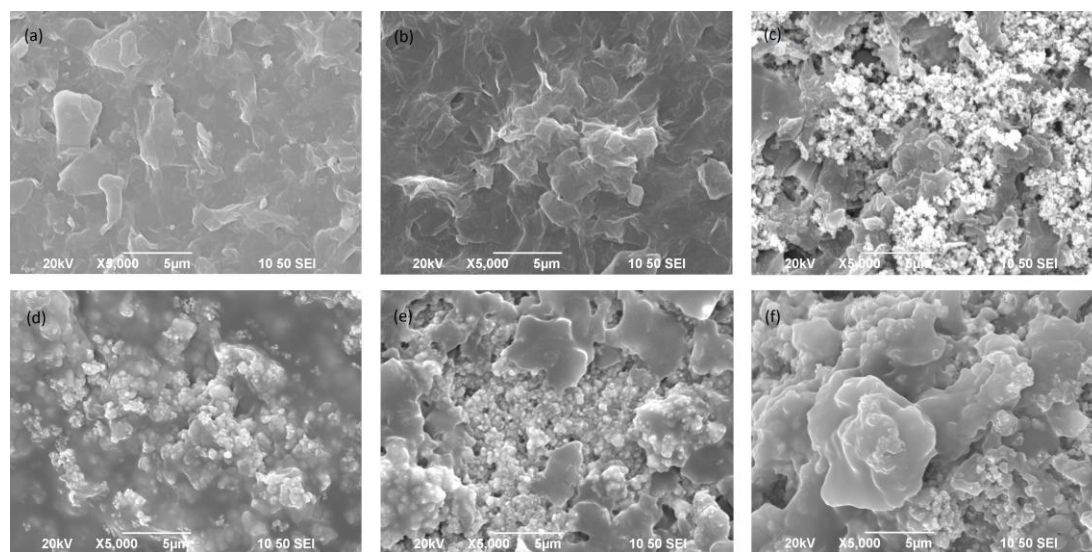


Fig. 2 SEM images of (a) GO, (b) R(A), (c) R(G)-SnO₂, (d) R(B)-SnO₂, (e) R(A)-SnO₂ and (f) R(H)-SnO₂.

hydrazine had the strongest reducing power of the tested reducing agents.

3.2. Raman analysis

The degrees of reduction of the GO, R(G), R(B), R(A) and R(H) were elucidated by Raman spectroscopy, as shown in Fig. 3. The characteristic vibrational D and G bands at $\sim 1,360$ and $\sim 1,590$ cm^{-1} , respectively, were observed in the GO and all of the RGO. The D band, representing a 'defect' signal, typically corresponds to the breathing-mode vibrations of the out-of-plane sp^3 carbon. The presence of a D band requires a breaking of the symmetry of the aromatic ring, as occurs in the sp^3 chair form of the ring or at edge sites. Hence, pristine graphite does not display this band. The G band, representing a pristine 'graphitic' signal, corresponds to the stretching-mode vibrations of the in-plane sp^2 carbon. After the reduction of the GO, the intensity ratio of I_D/I_G increased from 0.91 for R(G) to 1.01 in the case of R(H). This

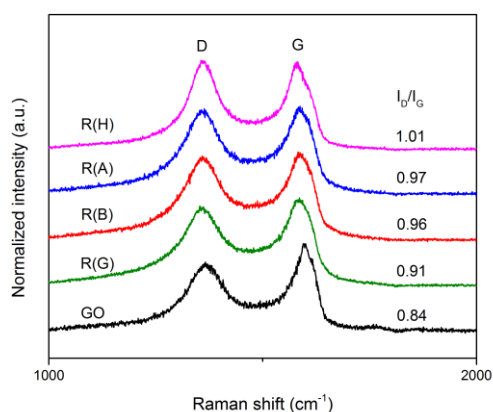


Fig. 3 Raman spectra of GO, R(G), R(B), R(A) and R(H).

increase in the D band signal relative to the G band was caused by the increased amounts of edge defects or in-plane carbon vacancies.^{31,32} Hence, an increase in the intensity ratio I_D/I_G indicated an increased degree of reduction. Fig. 3 shows that R(G) had the lowest degree of reduction ($I_D/I_G \sim 0.91$), while that of R(A) ($I_D/I_G \sim 0.97$) was slightly higher than R(B) ($I_D/I_G \sim 0.96$). R(H) had the highest degree of reduction ($I_D/I_G \sim 1.01$).

3.3. FTIR analysis

The functional-group compositions of the GO, R(G), R(B), R(A) and R(H) were elucidated by FTIR spectroscopy, as shown in Fig. 4. Strong bands at $1,750$ cm^{-1} (C=O), $1,280$ cm^{-1} (C-O-C), $1,064$ cm^{-1} (C-OH) and a broad band at $3,575$ cm^{-1} (O-H) were all observed in the GO, indicating the presence of oxygen functional groups including carbonyl, epoxy, carboxylic and hydroxyl. R(G) showed characteristic signals with intensities similar to those of the GO, indicating that the reducing power of glucose against these oxygen functional groups was very weak. However, the signals were strongly attenuated in R(B), R(A) and R(H), indicating that sodium borohydride, ascorbic acid and hydrazine hydrate were more powerful reducing agents than glucose. R(B) displayed low-intensity but broad signals of hydroxyl groups (O-H and C-OH), indicating that sodium borohydride was weak in reducing these groups. R(B), R(A) and R(H) all featured a small peak at $1,621$ cm^{-1} , corresponding to C=C, indicating that the sp^2 domain became more populated upon reduction. The C=C bond signals in R(A) and R(H) were stronger than that in R(B), indicating a greater degree of reduction. The signal at $1,280$ cm^{-1} (C-O-C) in the GO was up-shifted slightly to $1,336$ cm^{-1} in R(A) and R(H) due to the increased sp^2 content. However, the epoxy group (C-O-C) signal at $1,336$ cm^{-1} was stronger in R(A) than in R(B) and R(H), possibly due to the formation of dehydroascorbic acid (DHA) by the oxidation of ascorbic acid (A) after the reduction of the GO. The residual epoxy groups in DHA would thus have contributed to the relatively strong signal for C-O-C in R(A). The remaining oxygen functional groups, including carboxylic, epoxy and hydroxyl, were

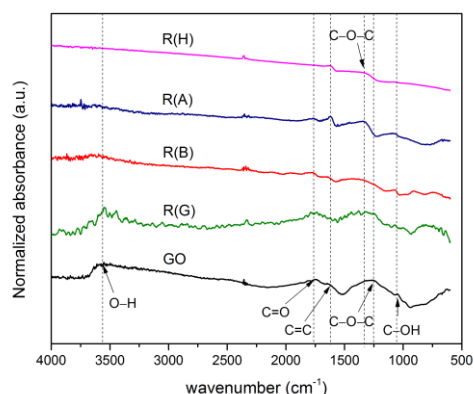


Fig. 4 FTIR spectra of GO, R(G), R(B), R(A) and R(H).

electron-withdrawing, allowing them to bind electron carriers at the surface, thus increasing the size of the space charge layer and the resistivity and gas sensitivity.⁴ These oxygen functional groups acted as active surface sites for the gases to attack, hence their effect on the resistance and gas response. The amount of oxygen functional groups remaining at the surface of the RGO after reduction was positively linked with their gas sensitivity (see the sensitivity tests in Section 3.5.2). Hence, R(G) and R(A) showed greater gas sensitivity than R(B) and R(H). However, R(A) showed a much higher degree of reduction than R(G), as discussed previously, indicating that ascorbic acid was the best reducing agent of the four candidates, having a higher reducing power as well as higher gas sensitivity.

3.4. XRD analysis

The crystalline structures of the GO, R(G), R(B), R(A) and R(H) and their heterostructures with SnO₂ were elucidated by XRD, as shown in Fig. 5. An intense signal of GO(002) at 9.06° was observed in the GO, corresponding to a d-spacing of 9.75 Å, as shown in Fig. 5(a). The increased d-spacing of the GO compared with the typical value of 3.35 Å in graphite was caused by the mutually repelling oxygen functional groups intercalated between the graphitic planes in the GO. Amorphous signals of RGO(002) at 23.88°, corresponding to a d-spacing of 3.72 Å, were observed in R(G), R(B), R(A) and R(H) due to the recovery of the π - π interaction between the graphitic planes by removing the electrostatically repelling oxygen functional groups in the GO. The d-spacing of 3.72 Å was still larger than the typical value of 3.35 Å in pristine graphite due to the incomplete removal of functional groups between graphitic planes. The intensity of GO(002) became weaker while the amorphous RGO(002) signal became stronger as the degree of reduction increased. Comparison of the relative intensity of GO(002) and RGO(002) showed that the degrees of reduction were in ascending order of R(G), R(B), (A) and R(H). The slight shifts of GO(002) to smaller angles from 9.06° to 8.48° (d-spacing ~10.41 Å) in R(G) and 7.32° (d-spacing ~12.06 Å) in R(B) could have been due to the intercalation of glucose and borohydride molecules, respectively, between the expanded graphitic planes. The shift in R(B) to a smaller angle than in R(G) could have been due to the formation of a large complex polynuclear borate after

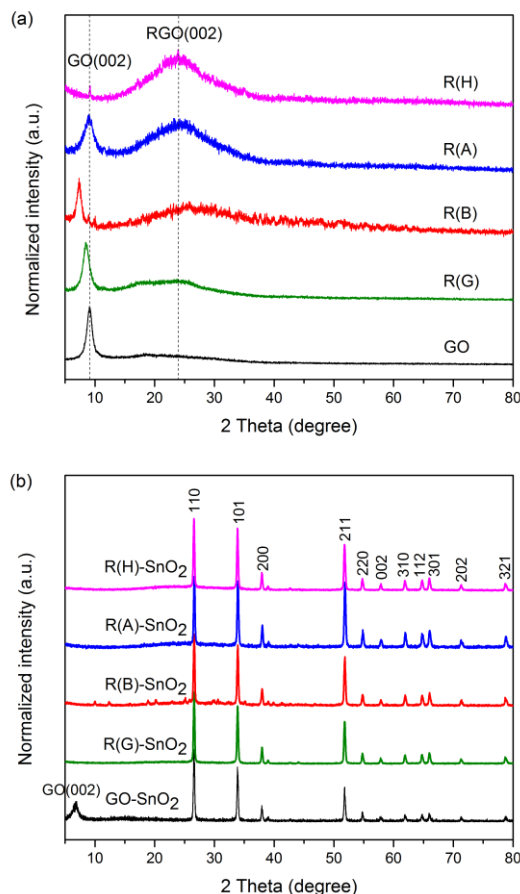


Fig. 5 XRD spectra of (a) GO, R(G), R(B), R(A) and R(H); (b) GO-SnO₂, R(G)-SnO₂, R(B)-SnO₂, R(A)-SnO₂ and R(H)-SnO₂.

hydrolysis of borohydride, further increasing the interplanar distance.³⁰ The shift of GO(002) to a smaller angle was not observed in R(A) and R(H) due to the stronger reducing power of ascorbic acid and hydrazine, such that the graphitic π - π interactions were strong enough to inhibit the intercalation of molecules between graphitic planes. The XRD spectra for the heterostructures of the GO, R(G), R(B), R(A) and R(H) with SnO₂ are shown in Fig. 5(b). The intense signals indicated by the indexes were caused by SnO₂ nanocrystallites. The strongest signal, at 26.58°, corresponds to the (110) plane, which is dominant in the SnO₂ crystalline structure. The signal of GO(002) was shifted to the smaller angle of 6.94° in GO-SnO₂ compared with the pure GO (9.06°) due to the intercalation of SnO₂ nanocrystallites between graphitic planes. However, the signals of GO(002) and RGO(002) were absent in all of the RGO heterostructures after the incorporation of SnO₂, which could be attributed to (1) the strong graphitic π - π interaction in RGO, which inhibited the intercalation of SnO₂ nanocrystals, or (2) the disordered stacking of RGO sheets in the composites, as observed in other work.³³

3.5. Electrical measurement

3.5.1. Resistance measurement

The electrical measurements of the resistance of the GO, R(G), R(B), R(A), R(H) and their heterostructures with SnO₂ at room temperature are shown in Fig. 6. The GO, a p-type material, had the highest resistance in this group due to the abundance of oxygen functional groups, which extracted and bound electrons to the surface, enlarging the space charge layer to reduce surface conductivity.¹⁵ Hence, resistance decreased for the increasing degree of reduction of the GO due to the removal of oxygen functional groups, which released the bound electrons back to the core. The resistances of the RGO were, in descending order, R(G), R(B), R(A) and R(H), consistent with the results from Raman, FTIR and XRD. The incorporation of SnO₂ into RGO increased the resistance by about one or two orders of magnitude due to the p-n junction effect at the contact boundary between the p-type RGO and n-type SnO₂.^{24,25} SnO₂ is n-type due to the introduction of free electrons at oxygen vacancy sites on the surface after annealing.³⁴ The n-type SnO₂ released its free electrons to the core and reduced the amount of free holes, which increased the resistance. The heterostructures were still p-type as a whole, as the number of free electrons released by SnO₂ was much less than the free holes in the RGO; oxygen in the air bound and extracted the free electrons at the vacancy defects of the SnO₂ surface, significantly decreasing the amount of electrons released back to the RGO core. Sensitivity measurements further confirmed that the heterostructures were p-type, as discussed in the next section. The larger increases of resistance in R(A)-SnO₂ and R(H)-SnO₂ (~ two orders of magnitude) than in R(G)-SnO₂ and R(B)-SnO₂ (~ one order of magnitude) could have been caused by the larger agglomerates of R(A) and R(H) with SnO₂, which resulted in more contact boundaries between RGO and SnO₂, thus strengthening the p-n junction effect.

3.5.2. Sensitivity measurement

The gas response, i.e., sensitivity, was measured in a homemade gas-testing chamber with a dynamic gas flow of 1% methane gas relative to the environmental air at room temperature.

Sensitivity was defined as $(R_g - R_a)/R_a$, where R_g is the resistance of the sample when the chamber was filled with methane gas, while R_a is the resistance of the sample when the chamber was purged of methane gas by environmental air. The sensitivity measurements of R(G), R(B), R(A) and R(H) and their heterostructures with SnO₂ towards methane at room temperature are depicted in Fig. 7. The sensitivities of all of the samples were positive due to the increase of resistance when the methane gas interacted with p-type samples. Methane is a reducing gas, which releases the bound electrons at the surface back to the core; hence, the number of holes in the RGO and RGO-SnO₂ decreased, increasing the resistance. R(G) had the highest sensitivity among the homostructures, as glucose had the weakest reducing power; most of the oxygen functional groups in R(G) remained for the methane gas to interact with. The sensitivity of R(G) was even higher than that of the GO, perhaps due to the residues of D-glucose remaining after reduction. After the reduction of the GO, D-glucose was oxidised to gluconic acid or the more stable ring form gluconic delta-lactone, both of which contained oxygen functional groups that further enlarged the space charge layer at the surface; therefore, the sensitivity was further increased by any residues of D-glucose. R(A) had a lower resistance than R(B), as shown in Fig. 6, so it was expected that R(A) would have a lower sensitivity than R(B). However, on the contrary, R(A) had a higher sensitivity than R(B), as shown in Fig. 7, a finding attributed to the residues of L-ascorbic acid. DHA, which was formed by the oxidation of L-ascorbic acid after the reduction of the GO, also contained oxygen functional groups, thus causing an increase in sensitivity. Most of the ascorbic acid was probably oxidised to DHA due to the high degree of reduction of R(A), as discussed previously. R(B) and R(H) had lower sensitivities than the other homostructures because the oxidative products of borohydride and hydrazine did not have oxygen functional groups to increase the sensitivity. R(H) had the lowest sensitivity of all, as hydrazine had the strongest reducing power; thus, most of the oxygen functional groups were removed, as

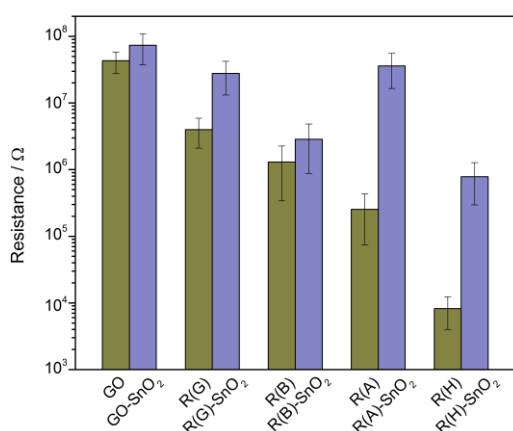


Fig. 6 Resistance of GO, R(G), R(B), R(A), R(H) and their heterostructures with SnO₂ at room temperature.

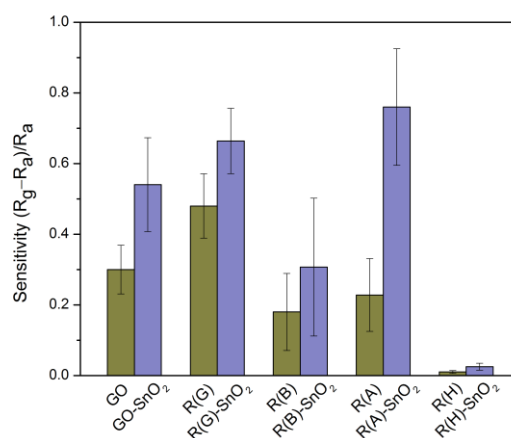


Fig. 7 Sensitivity of GO, R(G), R(B), R(A), R(H) and their heterostructures with SnO₂ towards methane (1%) at room temperature.

discussed previously. The sensitivity of R(H) increased after the incorporation of SnO₂, as observed in all of the heterostructures, due to the p-n junction effect, which enlarged the space charge layer to increase the responsiveness. Methane gas typically releases electrons back to the core when interacting with the adsorbed oxygen at vacancy defect sites on the surface of SnO₂. The release of electrons back to the p-type RGO decreases the amount of holes, thus increasing the resistance and sensitivity. R(H)-SnO₂ did not show a comparable increase of sensitivity to the other heterostructures, possibly because the increase of the Schottky barrier by the p-n junction was not significant and the sensitivity was instead dominated by the high conductivity of R(H). The distinctive increase of sensitivity of R(A)-SnO₂ compared with R(A) was caused by the synergistic effect between DHA (from the oxidation of ascorbic acid) and SnO₂, which is discussed in the next section. Figs. 8(a) and (b) show the sensitivity against time for the homostructures and heterostructures, respectively. Methane gas was forced out using environmental air when the sensitivity became saturated. The response time was defined as the time taken by the sensor to reach 90% of the saturated sensitivity. The response times of the gas sensors of the homostructures and their heterostructures were about 100–200 s.

Table 1 summarises the recent reports in the literature on room-temperature methane sensors compared with this work. The pure GO gas sensor had a higher sensitivity than doped graphene³⁸ or RGO⁴³ due to the abundant oxygen functional groups on the surface serving as active sites for gaseous interactions. Note that the sensing response and gas concentration are generally linear in log scale;^{44,45} hence, it is clear that our highest-performing sensor, R(A)-SnO₂, exhibited

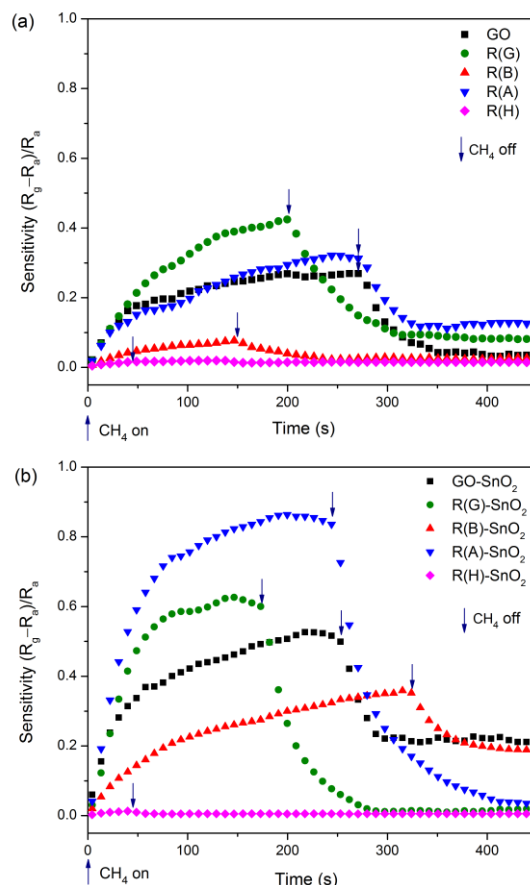


Fig. 8 Sensitivity against time plot of (a) GO, R(G), R(B), R(A) and R(H); (b) GO-SnO₂, R(G)-SnO₂, R(B)-SnO₂, R(A)-SnO₂ and R(H)-SnO₂ towards methane (1%) at room temperature.

Table 1 Recent reports on room temperature methane sensors.

Sensing material	Technique	CH ₄ conc.	Sensitivity	Year
CNT and CNF ³⁵	Electrolysis	10000 ppm	75%	2005
Pd/MWCNTs ³⁶	Chemical method	20,000 ppm	4.5%	2008
SnO ₂ nanorods ³⁷	Precipitation method	2500 ppm	0.58%	2012
Graphene/PANI ³⁸	Chemical method	3200 ppm	5%	2013
Pt/SWCNTs ³⁹	Electrochemical method	200 ppm	1.6%	2013
VO ₂ ⁴⁰	Pulsed dc sputtering	500 ppm	3.2% (50 °C)	2014
TiO ₂ /n-Si ⁴¹	rf sputtering	1000 ppm	16% (50°C)	2016
PbS colloidal nanocrystals ⁴²	Chemical method	50,000 ppm	47.6%	2016
Pd doped SnO ₂ /RGO ⁴³	Hydrothermal method	4000 ppm	2.07%	2016
GO	Chemical method	10,000 ppm	30%	Present work
R(A)/SnO ₂	Chemical method	10,000 ppm	76%	Present work

much better sensitivity (76%) than the metal oxide gas sensors and was comparable with a CNT sensor.³⁵ However, the sensitivity of the CNT sensor reached saturation near a methane concentration of 6,500 ppm, while the sensitivity of our R(A)/SnO₂ sensor continued to increase to 241% at 80,000 ppm. In addition, the fabrication of our sensors was both cheaper and more environmentally friendly.

3.6. DFT+U analysis

Section 3.5.2 states that the sensitivities of R(G) and R(A) were higher than that of the GO, as shown in Fig. 7, because the residues of glucose and ascorbic acid contained oxygen functional groups to enlarge the space charge layer at the surface. As the sensitivity of R(G) was higher than R(A), we expected that the sensitivity of R(G)-SnO₂ would be higher than R(A)-SnO₂ in their heterostructures. However, we found that R(A)-SnO₂ had the highest increase of sensitivity, possibly due to the synergistic effect between DHA and SnO₂, as mentioned

previously. To understand this effect more specifically, we performed DFT+U calculations on two systems: DHA-SnO₂ and Glucose-SnO₂. We did not consider borohydride and hydrazine systems in our calculations because the residues of borohydride and hydrazine after the reduction of the GO did not contain oxygen functional groups. As DFT calculations are quite demanding, we simplified our systems to include only the reducing agent and SnO₂ while excluding the RGO surface and gases for simplicity. It is believed that the RGO surface has more p-type character in R(G) than in R(A). Hence, R(G) should have a stronger p-n junction effect with SnO₂, which would induce higher sensitivity than R(A). However, the p-n junction effect in R(G)-SnO₂ was evidently outweighed by the synergistic effect between DHA and SnO₂ in R(A)-SnO₂, which induced higher sensitivity in the latter.

The (110) plane of SnO₂ is widely simulated in DFT calculations, as it is the most stable surface with the lowest energy.^{34,46} We observed that the (110) plane signal was the strongest peak in the XRD spectrum, as shown in Fig. 5 (b). The main features of the structure of SnO₂ in the (110) plane are illustrated in Fig. 9. Bulk SnO₂ has the rutile structure, such that each Sn is six-fold coordinated with O and each O is three-fold coordinated with Sn. However, due to the dangling bonds at the surface, there are two different lattice sites of Sn: Sn_{6c} (six-fold coordinated) and Sn_{5c} (five-fold coordinated). There are also two lattice sites of oxygen, i.e., 'bridging oxygen' and 'in-plane oxygen'. The two oxygen sites have different vacancy formation energies and electronic states.⁴⁷ The bridging oxygen is more unstable, so it has a smaller vacancy formation energy than in-plane oxygen. The oxygen vacancy defects are important in the formation of the n-type SnO₂ and also serve as high-energy active sites for gas sensing. The DFT calculations of our model showed that DHA and glucose were adsorbed at different sites on the SnO₂ surface, which had a significant effect on the sensing mechanism.

The CASTEP code was used to perform the DFT+U calculations.⁴⁸ In this framework, we used the rotationally invariant (Anisimov-type) DFT+U functional⁴⁹ and self-consistently determined Hubbard U parameter for the pseudised O-2p orbitals, based on our new linear response method.⁵⁰ The self-consistently determined Hubbard U potential was applied with U_p = 2.89 eV, a consensus value^{51–54} for many oxide materials. The PBE functional was chosen for the DFT+U calculations with a kinetic energy cutoff of 750 eV, and the valence electron states were expressed in a plane-wave basis set. The ensemble DFT (EDFT) method of Marzari et al.⁵⁵ was used for convergence. Reciprocal-space integration was performed using the special k-point (¼, ¼, 0)⁵⁶ with gamma-centre-off, which was self-consistently selected for total energy minimisation. With this special k-point, the total energy converged to less than 5.0 × 10⁻⁷ eV per atom. The Hellmann–Feynman forces on the atoms converged to less than 0.001 eV/Å. We used norm-conserving pseudopotentials generated using the OPIUM code in the Kleinman–Bylander projector form,⁵⁷ and used the non-linear partial core correction⁵⁸ and a scalar relativistic averaging scheme⁵⁹ to average the spin-orbital coupling effect. For this treatment, we chose a similar

non-linear core correction technique for correcting the valence–core charge density overlap in such elements. A detailed discussion of this method was presented in previous work on a native point-defect study of CeO₂.^{60,61} The RRKJ method was chosen to optimise the pseudopotentials.⁶² Prior to ab-initio predictions of the Hubbard U parameters for the orbitals, the geometries and lattice parameters of all of the SnO₂ (110) adsorption models were optimised using the PBE functional. This procedure reduced the computational cost and ensured the reliability of the Hubbard U value obtained by our self-consistent iterative calculations. We used this procedure before the Hubbard U determination, as DFT has been verified as reliable for the structural optimisation of compound solids with 4f or 5f orbitals,⁶³ even with ultrasoft pseudopotentials. This may be due to the well-developed pseudopotential technique,^{60,61,63} as shown by the small difference between the DFT and DFT+U calculated lattice parameters.^{50,54,60,61,64} Nevertheless, the U parameters had to be determined more carefully.^{50,54,60,61,64}

3.6.1. DHA-SnO₂ system

The structure of DHA is depicted in Fig. 10, which shows that the three carbonyl groups in the five-membered ring could be easily delocalised when interacting with an electron donor.⁶⁵ The DFT calculations revealed two particularly stable models of the DHA-SnO₂ system: models 1 (dissociated adsorption) and 2

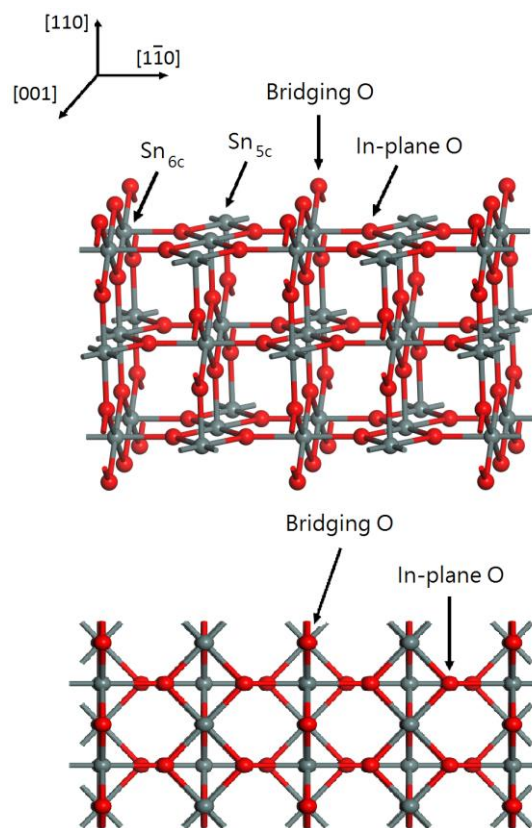


Fig. 9 (110) plane of SnO₂ surface.

Fig. 11
(dissociated)

(a)

(c)

DOS (a.u.)

Fig. 12
(undissociated)

(undissociated adsorption). The HOMO and LUMO of DHA on the (110) plane of SnO₂ in model 1 are shown in Figs. 11 (a) and (b), respectively. The formation energy E_{form} in the calculations was defined as $E_{\text{form}} = E_{\text{sys}} - \sum E_i$, where E_{sys} in model 1 is the energy of the whole system of DHA-SnO₂ and E_i comprises the isolated energies of DHA and SnO₂. The HOMO and LUMO of DHA were located at the five-membered ring of DHA, as shown in Figs. 11 (a) and (b), respectively. The five-membered ring and the 'tail' of DHA were dissociated with a formation energy E_{form} of -14.25 eV. The negative E_{form} indicated that the dissociation of DHA was exothermic, such that the dissociated DHA was stably adsorbed on SnO₂. From the density of states (DOS) plot shown in Fig. 11(c), the HOMO and LUMO energies of -0.871 and 0.014 eV, respectively, were separated by a non-zero DOS (the Fermi energy E_F is typically defined as 0); hence, there was no energy gap and hybridisation could occur easily, benefitting charge transfer. The five-membered ring was not adsorbed flat, but tilted from the plane, with carbonyl groups pointing downward towards the in-plane oxygen. This tilting might have been caused by the electron-donating property of the carbonyl groups, which were attracted towards the electron-withdrawing in-plane oxygen. The epoxy group in the ring was repelled upwards due to having the same electron-withdrawing nature as the in-plane oxygen. Other DFT calculations have reported that oxygen vacancies were mostly formed at the bridging oxygen sites rather than the in-plane oxygen sites,⁴⁷ in which case the dissociated DHA would not block the formation of these vacancy sites for gas adsorption. The band gap energy E_{gap} of 1.951 eV, as shown in Fig. 11(c), was calculated using the second-lowest unoccupied energy level.

Model 2, where no dissociation occurred, was determined as the most stable form of DHA on SnO₂. The HOMO and LUMO were again located at the five-membered ring of DHA, as shown in Figs. 12 (a) and (b), respectively. The formation energy E_{form} was determined as -12.87 eV, slightly less negative than that of model 1 (-14.25 eV). The negative E_{form} indicated that adsorption was again exothermic and favourable. Based on the DOS plot shown in Fig. 12(c), the HOMO (-0.667 eV) and LUMO (0.595 eV) were separated by a small band gap of 1.262 eV. Hence, hybridisation occurred easily for this narrow band gap at room temperature, benefitting charge transfer. The lower band gap energy for DHA in this model could have been caused by the delocalisation of the three carbonyl groups, as shown in Fig. 9. However, the DHA in model 2 was adsorbed flat on the SnO₂ surface, so that the electron-donating carbonyl groups could interact with the gas better than the downward-pointing carbonyl groups in model 1. Similarly, the adsorption position of DHA in model 2 was at the centre of the in-plane oxygen site,

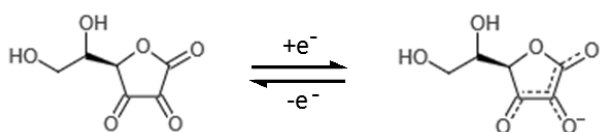


Fig. 10 Dehydroascorbic acid (DHA) and delocalization of the three carbonyl groups with an electron donor.

which would not block the bridging oxygen from forming vacancy defects, as observed in model 1. Hence, we attributed the synergistic effect between DHA and SnO₂ to the increased charge transfer from the delocalisation of the three carbonyl groups in the five-membered ring of DHA. As the electron-withdrawing in-plane oxygens were abundant on the SnO₂ surface, they induced greater charge transfer from the carbonyl groups in DHA when interacting with the reducing gas (methane). Delocalisation and charge transfer were not observed for the Glucose-SnO₂ system, which resulted in a lower sensitivity, as discussed in the next section.

3.6.2. Glucose-SnO₂ system

We have shown that glucose was the weakest reducing agent among those tested, as indicated by the Raman, FTIR and XRD spectra in the earlier sections. Hence, the residues of glucose mostly remained unoxidised after the reduction of the GO, with only a small fraction oxidised to gluconic delta-lactone. We performed DFT calculations for two models of the Glucose-SnO₂ system: models 3 (un-oxidised glucose-SnO₂) and 4 (gluconic delta-lactone-SnO₂). The structures of D-glucose (ring form) and gluconic delta-lactone are depicted in Figs. 13(a) and (b), respectively. Glucose and its derivative were modelled as the ring form in our DFT calculations, as this form was more stable than the chain form in non-aqueous states. The most stable adsorption state of D-glucose on SnO₂ was observed in model 3, with an E_{form} of -10.35 eV – less negative than that of the DHA system. The HOMO and LUMO were not close enough to allow hybridisation, as shown in Figs. 14(a) and (b), respectively. The band gap energy was determined as 5.410 eV, as shown in Fig. 14(c), confirming that the gap was too high for orbital hybridisation. (The small DOS around 2 eV was not identified as an effective LUMO state.) The less negative formation energy could have been caused by the adsorption site of glucose being atop the bridging oxygen rather than the in-plane oxygen. The attraction between glucose and bridging oxygen was evidently weaker than that between DHA and in-plane oxygen. In addition, the glucose contained no electron-donating carbonyl group to share orbitals and electrons as in the case of DHA, again resulting in a higher band gap energy and decreased charge transfer. Furthermore, the position of the adsorption site of glucose atop the bridging oxygen blocked the formation of vacancy defects and thus lowered the gas sensitivity. Thus, both the unfavourable adsorption site and high band gap energy of glucose contributed to making the gas sensitivity lower than that of the DHA-SnO₂ system.

The HOMO and LUMO of model 4 (gluconic delta-lactone-SnO₂) are shown in Figs. 15(a) and (b), respectively. The E_{form} of this system was determined as -9.46 eV, which was less

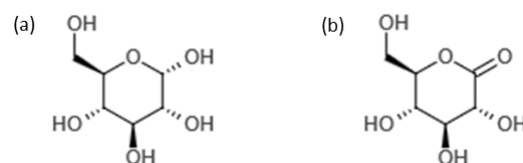


Fig. 13 (a) D-glucose (ring form) and (b) gluconic delta lactone

negative than that of model 3 due to the electron-withdrawing epoxy group being atop the in-plane oxygen, leading to an unfavourable mutual repulsion. The HOMO and LUMO overlapped at the carbonyl group. The band gap energy was determined as 4.285 eV, as shown in Fig. 15(c), which was again too high for hybridisation at room temperature. Similar to the DHA-SnO₂ system, the adsorption site of gluconic delta-lactone would not block the formation of vacancy defects at bridging oxygen sites, thus benefitting gas sensing. However, this model was of less practical relevance than model 3, as most of the glucose was not oxidised to gluconic delta-lactone, as mentioned previously.

4. Conclusions

In summary, the methane gas-sensing properties of the GO, R(G), R(B), R(A), R(H) and their heterostructures with SnO₂ at room temperature were studied. We found that (1) the degrees of reduction of the RGO were in ascending order of R(G), R(B), R(A) and R(H); (2) the gas sensitivities of the homostructures were in ascending order of R(H), R(B), R(A), GO and R(G); (3) the gas sensitivities of R(G) and R(A) were higher than those of R(B) and R(H) due to the residues of glucose/gluconic delta-lactone and DHA, respectively, on the RGO surface, which enlarged the space charge layer and thus improved the response; (4) the sensitivities of the heterostructures were in ascending order of R(H)-SnO₂, R(B)-SnO₂, GO-SnO₂, R(G)-SnO₂ and R(A)-SnO₂; and (5) the sensitivity of R(A)-SnO₂ was higher than that of R(G)-SnO₂ due to the synergistic effect between DHA and SnO₂, which induced greater charge transfer via orbital hybridisation at the carbonyl groups, and due to the more favourable adsorption site atop the in-plane oxygen. Our best-performing sensors were superior to most of the current room-temperature methane-sensing technologies, with a higher sensitivity, a wider sensing range, a lower fabrication cost and a lower environmental impact.

Acknowledgements

K. C. Lam would like to acknowledge his gratitude to K. S. Lo for his fruitful discussions throughout the project, and to the Hong Kong Polytechnic University for its financial support through a PhD scholarship and a research project (1-99QP).

References:

- J. F. McAleer, P. T. Moseley, J. O. Norris and D. E. Williams, *J. Chem. Soc. Faraday Trans. 1 Phys. Chem. Condens. Phases*, 1987, **83**, 1323–1346.
- J. F. McAleer, P. T. Moseley, J. O. Norris, D. E. Williams and B. C. Tofield, *J. Chem. Soc. Faraday Trans. 1 Phys. Chem. Condens. Phases*, 1988, **84**, 441–457.
- J. Watson, *Sens. Actuators*, 1984, **5**, 29–42.
- N. Yamazoe, *Sens. Actuators B Chem.*, 1991, **5**, 7–19.
- N. Yamazoe, Y. Kurokawa and T. Seiyama, *Sens. Actuators*, 1983, **4**, 283–289.
- S. R. Morrison, *Sens. Actuators*, 1987, **11**, 283–287.
- J. Allen Matthew, C. Tung Vincent and B. Kaner Richard, *Chem Rev*, 2010, **110**, 132–145.
- E. V. Iski, E. N. Yitamben, L. Gao and N. P. Guisinger, *Adv. Funct. Mater.*, 2013, **23**, 2554–2564.
- D. Chen, H. Zhang, Y. Liu and J. Li, *Energy Environ. Sci.*, 2013, **6**, 1362–1387.
- J. D. Fowler, M. J. Allen, V. C. Tung, Y. Yang, R. B. Kaner and B. H. Weiller, *ACS Nano*, 2009, **3**, 301–306.
- T. Gan and S. Hu, *Microchim. Acta*, 2011, **175**, 1–19.
- X. Li, H. Wang, J. T. Robinson, H. Sanchez, G. Diankov and H. Dai, *J. Am. Chem. Soc.*, 2009, **131**, 15939–15944.
- E. Llobet, *Sens. Actuators B Chem.*, 2013, **179**, 32–45.
- W. Yuan and G. Shi, *J. Mater. Chem. A*, 2013, **1**, 10078–10091.
- D. Chen, H. Feng and J. Li, *Chem. Rev.*, 2012, **112**, 6027–6053.
- K. Toda, R. Furue and S. Hayami, *Anal. Chim. Acta*, 2015, **878**, 43–53.
- F. Schedin, A. K. Geim, S. V. Morozov, E. W. Hill, P. Blake, M. I. Katsnelson and K. S. Novoselov, *Nat. Mater.*, 2007, **6**, 652–655.
- S. Pei and H.-M. Cheng, *Carbon*, 2012, **50**, 3210–3228.
- X. Gao, J. Jang and S. Nagase, *J. Phys. Chem. C*, 2009, **114**, 832–842.
- S. Park, J. An, J. R. Potts, A. Velamakanni, S. Murali and R. S. Ruoff, *Carbon*, 2011, **49**, 3019–3023.
- H.-J. Shin, K. K. Kim, A. Benayad, S.-M. Yoon, H. K. Park, I.-S. Jung, M. H. Jin, H.-K. Jeong, J. M. Kim, J.-Y. Choi and others, *Adv. Funct. Mater.*, 2009, **19**, 1987–1992.
- M. J. Fernandez-Merino, L. Guardia, J. I. Paredes, S. Villar-Rodil, P. Solis-Fernandez, A. Martinez-Alonso and J. M. D. Tascon, *J. Phys. Chem. C*, 2010, **114**, 6426–6432.
- C. Zhu, S. Guo, Y. Fang and S. Dong, *ACS Nano*, 2010, **4**, 2429–2437.
- S. Mao, S. Cui, G. Lu, K. Yu, Z. Wen and J. Chen, *J. Mater. Chem.*, 2012, **22**, 11009–11013.
- J.-H. Lee, A. Katoch, S.-W. Choi, J.-H. Kim, H. W. Kim and S. S. Kim, *ACS Appl. Mater. Interfaces*, 2015, **7**, 3101–3109.
- A. Takahashi, Y. Urano, K. Tokuhashi, H. Nagai, M. Kaise and S. Kondo, *J. Loss Prev. Process Ind.*, 1998, **11**, 353–360.
- P. A. Russo, N. Donato, S. G. Leonardi, S. Baek, D. E. Conte, G. Neri and N. Pinna, *Angew. Chem. Int. Ed.*, 2012, **51**, 11053–11057.
- L. Shahriary and A. A. Athawale, *Int J Renew Energy Env. Eng*, 2014, **2**, 58–63.
- R. F. Nickerson, *J. Appl. Polym. Sci.*, 1971, **15**, 111–116.
- R. K. Momii and N. H. Nachtrieb, *Inorg. Chem.*, 1967, **6**, 1189–1192.
- D. Luo, G. Zhang, J. Liu and X. Sun, *J. Phys. Chem. C*, 2011, **115**, 11327–11335.
- J. Shen, Y. Hu, M. Shi, X. Lu, C. Qin, C. Li and M. Ye, *Chem. Mater.*, 2009, **21**, 3514–3520.
- H. Song, L. Zhang, C. He, Y. Qu, Y. Tian and Y. Lv, *J. Mater. Chem.*, 2011, **21**, 5972–5977.
- V. Lantto, T. T. Rantala and T. S. Rantala, *J. Eur. Ceram. Soc.*, 2001, **21**, 1961–1965.
- R. K. Roy, M. P. Chowdhury and A. K. Pal, *Vacuum*, 2005, **77**, 223–229.
- Y. Li, H. Wang, Y. Chen and M. Yang, *Sens. Actuators B Chem.*, 2008, **132**, 155–158.
- A. Biaggi-Labiosa, F. Solá, M. Lebrón-Colón, L. J. Evans, J. C. Xu, G. Hunter, G. M. Berger and J. M. González, *Nanotechnology*, 2012, **23**, 455501.
- Z. Wu, X. Chen, S. Zhu, Z. Zhou, Y. Yao, W. Quan and B. Liu, *IEEE Sens. J.*, 2013, **13**, 777–782.
- E. Contes-de Jesus, D. Santiago, G. Casillas, A. Mayoral, C. Magen, M. José-Yacamán, J. Li and C. R. Cabrera, *J. Electrochem. Soc.*, 2013, **160**, H98–H104.
- A. K. Prasad, S. Amirthapandian, S. Dhara, S. Dash, N. Murali and A. K. Tyagi, *Sens. Actuators B Chem.*, 2014, **191**, 252–256.

- 41 B. Comert, N. Akin, M. Donmez, S. Saglam and S. Ozcelik, *IEEE Sens. J.*, 2016, **16**, 8890–8896.
- 42 A. Mosahebfard, H. Dehdashti Jahromi and M. H. Sheikhi, *IEEE Sens. J.*, 2016, **16**, 4174–4179.
- 43 S. Nasresfahani, M. H. Sheikhi, M. Tohidi and A. Zarifkar, in *Electrical Engineering (ICEE), 2016 24th Iranian Conference on*, IEEE, 2016, pp. 1014–1018.
- 44 H. Wang, Y. Qu, H. Chen, Z. Lin and K. Dai, *Sens. Actuators B Chem.*, 2014, **201**, 153–159.
- 45 J. Hu, F. Gao, Z. Zhao, S. Sang, P. Li, W. Zhang, X. Zhou and Y. Chen, *Appl. Surf. Sci.*, 2016, **363**, 181–188.
- 46 J. Oviedo and M. J. Gillan, *Surf. Sci.*, 2000, **463**, 93–101.
- 47 J. Oviedo and M. J. Gillan, *Surf. Sci.*, 2000, **467**, 35–48.
- 48 S. J. Clark, M. D. Segall, C. J. Pickard, P. J. Hasnip, M. I. Probert, K. Refson and M. C. Payne, *Z. Für Krist.-Cryst. Mater.*, 2005, **220**, 567–570.
- 49 V. I. Anisimov, F. Aryasetiawan and A. I. Lichtenstein, *J. Phys. Condens. Matter*, 1997, **9**, 767.
- 50 B. Huang, *J. Comput. Chem.*, 2016, **37**, 825–835.
- 51 S. Lany and A. Zunger, *Phys. Rev. B*, 2009, **80**, 85202.
- 52 S. Lany and A. Zunger, *Phys. Rev. B*, 2010, **81**, 205209.
- 53 B. J. Morgan and G. W. Watson, *J. Phys. Chem. C*, 2010, **114**, 2321–2328.
- 54 P. R. Keating, D. O. Scanlon, B. J. Morgan, N. M. Galea and G. W. Watson, *J. Phys. Chem. C*, 2012, **116**, 2443–2452.
- 55 N. Marzari, D. Vanderbilt and M. C. Payne, *Phys. Rev. Lett.*, 1997, **79**, 1337.
- 56 M. I. J. Probert and M. C. Payne, *Phys. Rev. B*, 2003, **67**, 75204.
- 57 L. Kleinman and D. M. Bylander, *Phys. Rev. Lett.*, 1982, **48**, 1425.
- 58 S. G. Louie, S. Froyen and M. L. Cohen, *Phys. Rev. B*, 1982, **26**, 1738.
- 59 I. Grinberg, N. J. Ramer and A. M. Rappe, *Phys. Rev. B*, 2000, **62**, 2311.
- 60 B. Huang, R. Gillen and J. Robertson, *J. Phys. Chem. C*, 2014, **118**, 24248–24256.
- 61 B. Huang, *Philos. Mag.*, 2014, **94**, 3052–3071.
- 62 A. M. Rappe, K. M. Rabe, E. Kaxiras and J. D. Joannopoulos, *Phys. Rev. B*, 1990, **41**, 1227.
- 63 C. J. Pickard, B. Winkler, R. K. Chen, M. C. Payne, M. H. Lee, J. S. Lin, J. A. White, V. Milman and D. Vanderbilt, *Phys. Rev. Lett.*, 2000, **85**, 5122.
- 64 T. Zacherle, A. Schriever, R. A. De Souza and M. Martin, *Phys. Rev. B*, 2013, **87**, 134104.
- 65 J. R. Juhasz, L. F. Pisterzi, D. M. Gasparro, D. R. Almeida and I. G. Csizmadia, *J. Mol. Struct. THEOCHEM*, 2003, **666**, 401–407.